Progress in Additive Manufacturing
https://doi.org/10.1007/s40964-024-00600-5

FULL RESEARCH ARTICLE

Influence of part temperature on in-situ monitoring of powder bed fusion of metals using eddy current testing

Marvin A. Spurek[1,2] · Adriaan B. Spierings[1] · Marc Lany[3,4] · Bernard Revaz[3,4] · Gilles Santi[3,4] · Jonatan Wicht[3,4] · Konrad Wegener[2]

Received: 27 November 2023 / Accepted: 8 March 2024

Abstract
Powder bed fusion of metals (PBF-LB/M) is currently the most widely adopted additive manufacturing technology for the fabrication of metal parts. However, the inconsistent quality of PBF-LB/M-manufactured parts and high costs for part certification are impeding wider industrial adoption. In-situ monitoring technologies are expected to enable process control in order to ensure consistent quality, and to replace some of the post-process inspection steps, therefore, reducing part certification costs. Eddy current testing (ECT) is a standardized nondestructive testing technique, which can be used as an in-situ monitoring technology to measure the part quality during the PBF-LB/M build cycle. However, the process-induced complex temperature fields in PBF-LB/M parts during the build cycle are among the most relevant disturbances due to the temperature dependence of the electrical conductivity. This study investigates the process-induced temperature influence on in-situ monitoring of relative density using ECT. Parts made from AlSi10Mg were manufactured on a PBF-LB/M machine and the build cycle was monitored using ECT and an infrared camera, which was used to extract the part surface temperature right before the ECT measurement. The results demonstrate that the temperature increase of the parts during the build cycle decreases the electrical conductivity independently of the relative part density, which was measured via micro-computed tomography. Therefore, a temperature compensation method was proposed and applied demonstrating that a layer-to-layer difference of 0.15 % relative density can be detected via ECT. Consequently, it has been demonstrated that ECT is an effective in-situ monitoring technology for PBF-LB/M, even in the presence of temperature disparities within parts.

Keywords Powder bed fusion of metals (PBF-LB/M) · Eddy current testing (ECT) · In-situ monitoring · Thermography · In-situ temperature measurement

1 Introduction

Powder bed fusion of metals (PBF-LB/M) is currently the most widely adopted additive manufacturing technology for fabricating metal parts [1]. Among the most important industries adopting PBF-LB/M are medical [2] and aerospace [3], where PBF-LB/M enables the manufacturing of individualized and complex-shaped parts, and parts with superior material performance relative to their weight, respectively. These industries require consistent and high part quality ensured by rigorous quality standards and, respectively, required part certificates owing to their safety-critical applications. According to Wei et al. [4], there is a large time lag between the design and certification of PBF-LB/M-manufactured parts as reproducible manufacturing of defect-free and structurally sound parts is still challenging. Determining suitable process conditions to obtain process qualification and part certification, therefore, requires extensive trial and error testing including destructive and nondestructive testing (NDT) of PBF-LB/M-manufactured parts during post-processing. Not only are these tests costly, but depending on the region of interest within the part volume

✉ Marvin A. Spurek
mspurek@ethz.ch

[1] inspire AG, Innovation Center for Additive Manufacturing Switzerland (icams), Fürstenlandstrasse 122, 9014 St. Gallen, Switzerland

[2] Swiss Federal Institute of Technology, ETH Zurich, Institute of Machine Tools and Manufacturing (IWF), Leonhardstrasse 21, 8092 Zurich, Switzerland

[3] Sensima Inspection SARL, 2 Route Cité Ouest, 1196 Gland, Switzerland

[4] AMiquam SA, 2 Route Cité Ouest, 1196 Gland, Switzerland

Published online: 10 April 2024

and the alloy used, it can be very challenging to reliably detect the required defect types and characteristics due to the limitations of the respective testing methods. For example, reliably detecting small defects in the center of large parts made from dense metals via X-ray micro-computed tomography (μCT) is difficult owing to the absorption of X-rays [5]. Consequently, a brute-force approach to qualify the PBF-LB/M process and to certify PBF-LB/M-manufactured parts typically has to be conducted per machine, feedstock material, and part geometry ultimately accounting for a significant proportion of the overall manufacturing costs per part which still impede the wider industrial adoption of PBF-LB/M [6].

In the future, in-situ monitoring technologies are expected to enable process control contributing to higher reproducibility of part quality, and to support or even replace some of the post-process inspection steps as discussed by Debroy et al. [6]. Therefore, tremendous effort was put into research and development of in-situ monitoring technologies in recent years reflected by the increase in related papers published pointed out by Grasso et al. [7]. While the majority of in-situ monitoring technologies are indirect techniques primarily focused on extracting process signatures and detecting anomalies within these signatures [7], there is a growing number of studies on developing established NDT technologies for in-situ inspection during the PBF-LB/M process. The benefits of employing these technologies as in-situ inspection techniques include their extensive industrial adoption for post-process inspection, their acceptance among users in the industry, and the availability of established standards and methodologies for generating part certificates during post-processing, which can be utilized for this purpose. One of these promising NDT technologies is eddy current testing (ECT) as the hardware is relatively inexpensive, and according to ASTM E3166-20 [8] it can be used to detect several relevant discontinuity classes in PBF-LB/M-manufactured parts: surface features, porosity, cracking, lack of fusion, inclusions and residual stress. The majority of research on the adoption of ECT to PBF-LB/M is focused on evaluating the ability to detect different designed defects in the near-surface region of PBF-LB/M parts after the build cycle has been completed and the respective parts have been removed from the PBF-LB/M machine. The studies primarily use parts with designed cavities of different sizes and shapes as exemplified in [9–17], and porosity triggered by intentional degradation of process parameters as demonstrated in [18–20]. However, there are only few studies on the adoption of ECT as an in-situ technique measuring the layerwise solidified material during the PBF-LB/M build cycle where the ECT system is mounted on the recoater of the PBF-LB/M machine [21–23]. This approach enables to extend the testable area from the near-surface region of the part as described in ASTM E3166-20 [8] to the full part volume. However, it requires sophisticated signal processing methods to layerwise segment the ECT data and subsequently spatially match the layerwise segmented data with post-process μCT data in order to establish defect detection algorithms as demonstrated by Spurek et al. [22].

Although ECT can generally be used in harsh environments and the aforementioned studies demonstrate the capability of in-situ monitoring of PBF-LB/M using ECT, the physics of the PBF-LB/M process impose several challenges among which the complex temperature fields in PBF-LB/M parts during the build cycle are expected to be one of the most critical ones as discussed by John et al. [24]. According to Wei et al. [4] and Mukherjee et al. [25], the temperature fields, cooling rates, and temperature gradients in PBF-LB/M highly depend on the alloy, process parameters, and part geometry used. Furthermore, Williams et al. [26] demonstrated that the inter-layer cooling time, i.e., the time between the laser illumination of two subsequent layers, affects the evolution of the part surface temperature during the build cycle. In addition, independent of the inter-layer cooling time, a significant increase of the part surface temperature as a function of the build height was demonstrated. This is owing to the cold start of the PBF-LB/M build cycle and the layer-to-layer heat input by the laser beam until an equilibrium with the heat loss, i.e., predominantly heat conduction to the build plate [4], is established throughout the build cycle as pointed out by Williams et al. [26]. Hence, the part geometry, process parameters, build height, build cycle details, i.e., number of parts, support structures, nesting, and sequence of part illumination, among others, will possibly lead to spatial temperature differences in the solidified material while the in-situ ECT measurement is conducted. The adoption of ECT for in-situ monitoring of PBF-LB/M relies on measuring the electrical conductivity of predominantly paramagnetic alloys and utilizing calibration models leveraging correlations between the measured electrical conductivity and defect characteristics within the corresponding material volume in space as demonstrated by Spurek et al. [22]. Since the electrical conductivity of metals is inversely related to their temperature [27], the aforementioned spatial temperature differences within parts and between parts disturb the ECT measurement as spatial differences in temperature affect the electrical conductivity and can, therefore, be misinterpreted as defect signatures. The influence of sample temperature variation on the electrical conductivity measurement via ECT is well known in the literature [27] and the corresponding change in electrical conductivity is calculated using a linear approximation according to

$$\sigma(T) = \sigma(T_0)\,[1 + \alpha\,\Delta T] \tag{1}$$

$\sigma(T)$, $\sigma(T_0)$, α and ΔT denote the corrected electrical conductivity at temperature T, the electrical conductivity at reference temperature T_0, the temperature coefficient of the electrical conductivity of the alloy, and the temperature difference $\Delta T = T - T_0$, respectively. Given $\sigma(T_0)$, α and ΔT, the temperature-induced measurement error can, therefore, be reduced using Eq. (1). However, when it comes to PBF-LB/M, it should be noted that, for the majority of the alloys, both α and σ values are typically not known. The alpha value is usually established empirically, whereas the σ value can be influenced by various process parameters as well as build orientation, as demonstrated by Silbernagel et al. [28]. Furthermore, it is not straightforward to obtain ΔT as determining the actual part surface temperature during the build cycle usually requires a sophisticated calibration of the, respectively, used temperature sensors as demonstrated by Williams et al. [29].

This study investigates the impact of process-induced part temperature differences on in-situ monitoring of PBF-LB/M using eddy current testing and proposes a suitable temperature compensation method. Therefore, high cuboid parts made from AlSi10Mg are manufactured on a PBF-LB/M machine to trigger the aforementioned part surface temperature increase as a function of the build height demonstrated by Williams et al. [26]. The parts are in-situ monitored during the build cycle by an ECT system and a calibrated infrared camera. The layerwise relative electrical conductivity per part is then extracted from the ECT data and compared to the corresponding layer-to-layer relative density determined via post-process µCT analysis. Subsequently, the layer-to-layer part surface temperature at the moment of the ECT measurement is extracted from the infrared camera data. Based on these data, a temperature compensation method is developed and the performance is evaluated by comparing the resulting accuracy of the layerwise relative density measurement via ECT to the case without temperature compensation.

2 Materials and methods

2.1 Experimental setup and build cycle

The experiments were carried out on an AconityMIDI+ PBF-LB/M machine (Aconity3D GmbH, Herzogenrath, Germany) equipped with an Nd–YAG fiber laser with a maximum continuous laser power of 400 W. The recoater was modified as presented in Fig. 1a. The ECT measurement equipment was mounted on the opposite side of the brush holder on the recoater enabling to layerwise measure manufactured parts during the normal powder recoating process without modification of the build cycle. The ECT measurement was carried out adopting an Ultra-Portable Eddy Current (UPEC) instrument to which the ECT sensor, a ferrite pot core coil ($L = 80\ \mu$H) with an outer diameter of $d_c = 5.8\ mm$ (both Sensima Inspection Sarl, Gland, Switzerland), was connected in a bridge configuration. Further details on the system and machine integration are described by Spurek et al. [22]. The ECT sensor was positioned at a distance of 500 μm to the build plate surface before starting the build cycle as shown in Fig. 1b. The distance increases to the nominal lift-off L_n due to the layer-to-layer increase of the solidified layer thickness at the start of the build cycle

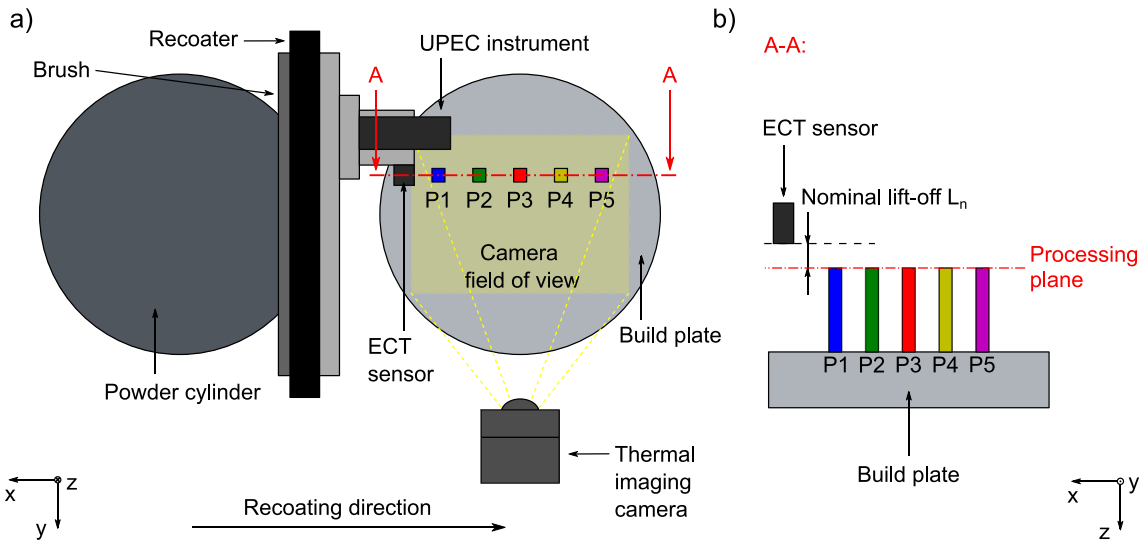

Fig. 1 Schematic illustration of the experimental setup and the build cycle. **a** Integration of the ECT system and the infrared camera into the AconityMidi+ build chamber. **b** Cross-sectional view illustrating the distance between the ECT sensor and part surface

until the nominal solidified layer thickness is reached after $10-12$ layers as demonstrated by Spurek et al. [22].

An Optris PI 640i infrared camera (Optris GmbH, Berlin, Germany) with a resolution of 640×480 pixels, a field of view of $33° \times 25°$ and a sampling rate of 32 Hz was mounted into the build chamber of the AconityMIDI+ PBF-LB/M machine as illustrated in Fig. 1a. To protect the camera from process by-products such as fumes, it was mounted within a customized housing and views the build area through a zinc sulfide window (Edmund Optics, Inc., Barrington, NJ, USA), which allows transmission within the wavelength range of 400–10,000 nm. The integration ensured that the majority of the build area was within the field of view. The camera focus was adjusted to ensure the center of the manufactured samples was in the focal plane of the camera albeit the distortion owing to the viewing angle of about 45° due to the mounting position of the infrared camera. The camera was connected to an acquisition computer outside of the build chamber on which the acquisition software Optris PI Connect (Optris GmbH, Berlin, Germany) was running, and the acquired data were stored.

Five parts with dimensions $10 \times 10 \times 60\ mm^3$ were positioned according to Fig. 1a and manufactured with the process parameters presented in Table 1. Gas atomized AlSi10Mg powder (Carpenter Technology Corp., Philadelphia, PA, USA) with a particle size distribution of $10-60\ \mu m$ was used as feedstock material, which was dried for 24 h under vacuum at 60 °C prior to processing. All parts were fabricated without support structures onto an AlSi1MgMn build plate and afterwards removed by wire cutting.

2.2 In-situ eddy current testing

The eddy current measurement principle is explained exhaustively by Bowler [27]. Furthermore, Spurek et al. [22] explain the aspects that are important when adopting ECT as an in-situ monitoring technique for PBF-LB/M. In principle, ECT utilizes the induction of eddy currents in testable metal samples owing to a time-varying primary magnetic field triggered by an alternating current, which runs through a coil brought in close proximity to the sample. The induced eddy currents generate a secondary magnetic field opposing the primary one, triggering a change in coil impedance, which is measured by the ECT instrument. The inspection depth in the sample is defined as the standard penetration depth [30], which is calculated according to

$$\delta = \frac{1}{\sqrt{\pi f \sigma \mu}} \tag{2}$$

where f, σ, $\mu = \mu_0 \mu_r$ denote the excitation frequency, the electrical conductivity and the magnetic permeability of the material, respectively, and where μ_r is the relative magnetic permeability and $\mu_0 = 1.256 \cdot 10^6\ H/m$ is the magnetic permeability in vacuum [27]. According to Eq. (2), the penetration depth of the eddy currents can be adjusted by setting a suitable excitation frequency f. Within this study, an excitation frequency of $f = 200\ kHz$ was selected yielding $\delta = 313\ \mu m$ in AlSi10Mg, given $\sigma = 12.85\ MSm^{-1}$ [28] and $\mu_r = 1.00$ [27].

The ECT signals were continuously acquired during the PBF-LB/M build cycle using a sampling rate of $f_s = 375\ Hz$ yielding a point spacing of $\Delta x = v_r / f_s = 0.26\ mm$ given the recoating speed of $v_r = 100\ mm/s$ (see Table 1). The ECT signals were then layerwise segmented, i.e., the respective fraction of the time series was matched with the corresponding layer index of the PBF-LB/M build cycle. Subsequently, the recoater position information provided by the axis encoder was used to extract the ECT signals when moving across the center region of each part, specified by the encoder range $\Delta x_p = 3\ mm$, to exclude a potential influence by the part edges. The resulting part- and layerwise segmented ECT signals were then transformed according to the method developed by Spurek et al. [22], which allows to calculate the relative electrical conductivity σ_r. Hereby,

Table 1 PBF-LB/M process parameters

Parameter			
Scan speed (P1–P5)	v_s	[mm/s]	1500, 1800, 1915, 2015, 2100
Hatch distance	h_s	[µm]	100
Laser power	P_L	[W]	380
Layer thickness	$t_{l,n}$	[µm]	60
Laser spot diameter	d_s	[µm]	105
Scan pattern		–	90° alternating
Recoater type		–	Silicone-reinforced carbon fiber brush
Recoating speed	v_r	[mm/s]	100
Shielding gas		–	Nitrogen
Chamber oxygen content		[ppm]	< 1000
Chamber overpressure		[mbar]	60

σ_r corresponds to the electrical conductivity relative to the electrical conductivity of the final layer of part P1 where $\sigma_r = 100$ %. Finally, the means and standard deviations of σ_r per part and layer were calculated.

Before conducting in-situ measurements, the level of uncertainty in σ_r arising from the ECT instrument noise was quantified according to the principle of the expanded uncertainty explained in [31] as $U_I = k \cdot \sigma_n \cdot n^{-0.5} = 0.03$ %, expressed in units of σ_r. Hereby, $k = 3$, $\sigma_n = 0.0321$ % (expressed in units of σ_r), $n = 11$ denote the coverage factor referring to a confidence level of 99.7 %, the standard deviation of the ECT instrument noise and the sample size per layer acquired within Δx_p, respectively.

2.3 In-situ full-field infrared monitoring

In order to measure the part temperature during the build cycle, the infrared camera requires calibration. Although the commonly adopted calibrating method using blackbody sources at known temperatures accounts for the camera sensor's non-linear response, it does not consider the actual emissivity of the target object as discussed by Williams et al. [26]. The emissivity ϵ is the efficiency of a body to emit thermal radiation and is defined as the ratio of energy radiated from a material's surface to that radiated from a blackbody [32]. The emissivity is a dimensionless number between 0 and 1, where 0 is considered a perfect reflector and 1 a perfect emitter. According to Williams et al. [26], the emissivity of a metal part will depend on the alloy used, the temperature, the surface roughness, the oxidation of the surface, and the view angle, among others.

The build scenario used in this study (see Sect. 2.2) contains 5 parts manufactured with different process parameters at different locations on the build plate. The different locations on the build plate translate to different camera view angles, and the different process parameters have an effect on the surface roughness according to Debroy et al. [6] both affecting the emissivity as previously discussed. Thus, in contrast to the build scenario of Williams et al. [26], each part with its unique location and process parameter must be calibrated independently in this study. Therefore, 5 geometrically identical calibration parts with the dimensions $10 \times 10 \times 10\ mm^3$ (C1–5, see Fig. 2a)) were manufactured at the same build location using the same machine, feedstock material, and process parameters yielding similar surface roughness, therefore, similar emissivity as the parts to be investigated. After finishing the build cycle, the excess powder was removed and 5TC-GG-KI-30-1M K-type thermocouples (Omega Engineering Inc., Norwalk, CT, USA) were attached to a designed notch with dimensions $4 \times 1.5 \times 1.5\ mm^3$ on the top surface of each calibration part using thermal paste as shown in Fig. 2a). The thermocouples were connected to USB-TC01 thermocouple measurement devices (National Instruments Corp., Austin, TX, USA) placed outside of the build chamber which were connected to an acquisition computer to log the temperature during calibration. During the calibration procedure, the build plate piston position was kept constant, hence the top surfaces of the calibration parts still lie in the PBF-LB/M process plane. The build chamber was then flooded with Nitrogen until an oxygen content of < 1000 ppm was reached, which is similar to the oxygen content during the PBF-LB/M process (see Table 1).

The calibration parts were then heated up using an inductive heating unit (Aconity GmbH, Herzogenrath, Germany), which was sequentially set to the following heating

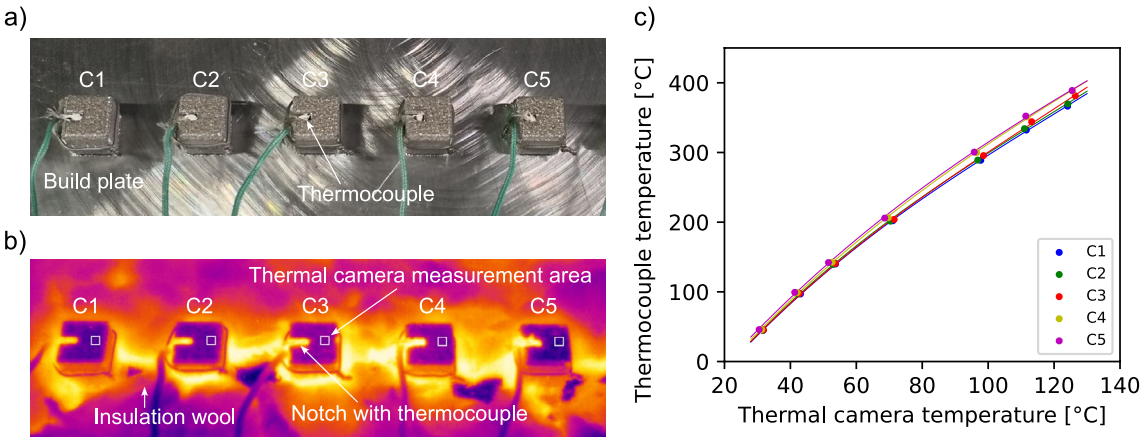

Fig. 2 **a** Build plate with 5 PBF-LB/M-manufactured calibration parts (C1–5) with thermocouples placed in notches at each part's surface. **b** Infrared camera image showing C1–5 during heat up as part of the calibration procedure. **c** Thermocouple temperature plotted against the infrared camera temperature ($\epsilon = 1$), both averaged during $t_m = 60\ s$ at different heating temperatures $T_h = \{35, 70, 100, 150, 250, 350, 500\}$ [°C]. Calibration functions were obtained by fitting 3rd-order polynomial functions to the data with $R^2 > 0.99$ per calibration part, respectively

temperatures: $T_h = \{35, 70, 100, 150, 250, 350, 500\}$ [°C] as shown in Fig. 2b). After the temperature reading of the thermocouples stabilized at each temperature level, the temperature was recorded using the infrared camera, and the data was logged from the thermocouples for a measurement duration $t_m = 60\,s$, respectively. The infrared camera reading is performed on a 8×8 pixels area on each part as depicted in Fig. 2b) and the temperature within the area averaged to mitigate pixel-to-pixel variations owing to local variation in surface roughness on each part surface. As the Optris PI Connect acquisition software requires setting an emissivity value, it was set to 1 for all parts, i.e., reported uncalibrated temperatures measured by the infrared camera correspond to the emissions of a blackbody source. Subsequently, the measurement data acquired via the thermocouples and the infrared camera at each temperature level T_h were, respectively, averaged and the results plotted against each other as presented in Fig. 2c). Unique calibration curves per calibration part, i.e., per PBF-LB/M process parameter and part location, were then obtained by fitting 3rd-order polynomial functions (all $R^2 > 0.99$). These calibration functions allow to translate the respective part temperature recorded by the infrared camera to the actual part temperature measured by the thermocouples. Hence, the empirically obtained calibration functions enable to account for the non-linearity of the emissivity as a function of temperature, and the differences in emissivity owing to different PBF-LB/M process parameters and locations on the build plate.

2.4 X-ray micro-computed tomography

X-ray micro-computed tomography (µCT) scans of the parts were obtained using a Zeiss Metrotom 1500 G3 system (Carl Zeiss AG, Jena, Germany) which was operated at 177 kV and 69 µA yielding a voxel size of 12 µm. According to Du Plessis et al. [5] the smallest detectable pore has a size of approximately $3 \times 3 \times 3 = 27$ voxels. Therefore, the smallest detected pore diameter is approximately 36 µm. The porosity analysis was carried out using the VGDefX algorithm of the software VGSTUDIO MAX 3.5 (Volume Graphics GmbH, Heidelberg, Germany). The resulting porosity matrices per part containing the sphericity, location, and equivalent spherical pore diameter, i.e., the diameter of a sphere with the defect volume, were exported and subsequently analyzed. Hereby, the sphericity Φ is calculated according to $\Phi = A_s \cdot A_d^{-1}$ where A_d and A_s denote the surface area of the defect and the surface area of a sphere with equivalent volume, respectively.

Subsequently, image stacks per part with an image-to-image distance in the z-direction of $d_{im} = 10\ \mu m$ were exported. In order to layerwise compare the ECT signals with the relative density of the corresponding material volume obtained via µCT, the method developed by Spurek et al. [22] was adopted, where each slice corresponds to the material volume that was layerwise measured by ECT during the PBF-LB/M build cycle $V_s = w_s \cdot l_s \cdot \delta^* = d_c \cdot (\Delta x_p + d_c) \cdot \delta^*$. As shown in Fig. 3, w_s, l_s, δ^*, d_c, Δx_p denote the slice

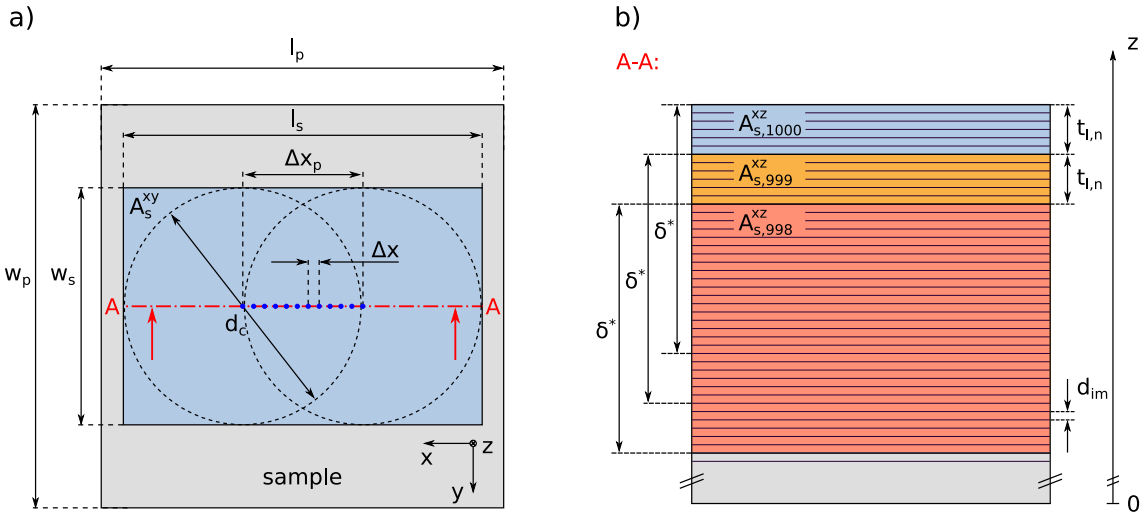

Fig. 3 Spatial matching of ECT and µCT data. **a** Top view where $l_p = 10\,mm$, $l_s = 8.78\,mm$, $w_p = 10\,mm$, $w_s = 5.8\,mm$, A_s^{xy}, $d_c = 5.8\,mm$, $\Delta x = 0.26\,mm$, Δx_p denote the part length, slice length, part width, slice width, the slice area in the xy-plane, the outer coil diameter, the point spacing and the selected encoder range at the center region of the part, respectively. **b** Cross-sectional view (xz-plane) of the top 3 slices ($i \in \{998, 999, 1000\}$) where $A_{s,i}^{xz}$, δ^*, $t_{l,n}$, d_{im} denote the slice area in the xz-plane, the respective penetration depth of the eddy currents (rounded off to the nearest tenth), the layer thickness and the distance between subsequent images j, respectively. Figure adapted from Spurek et al. [22]

width, the slice length, the ECT standard penetration depth (rounded to the nearest tenth), the nominal layer thickness, the outer coil diameter and the selected encoder range at the center region of the part, respectively. Given $\delta^* = 310\ \mu m$ and $t_{l,n} = 60\ \mu m$, the relative density per slice $\rho_{s,i}$ was determined according to

$$\rho_{s,i} = 1 - \left(\frac{d_{im}}{\delta^*} \sum_{j=d_{im}^{-1}(it_{l,n}-\delta^*)}^{it_{l,n}d_{im}^{-1}} \frac{A_{d,j}}{A_s} \right) = 1 - \left(\frac{1}{31} \sum_{j=6i-31}^{6i} \frac{A_{d,j}}{A_s} \right) \tag{3}$$

$\{i \in \mathbb{N} \mid 50 \leq i \leq 1000\}$, j, $A_{d,j}$, A_s denote the layer index, the image index in the image stack, the pore area of image j and the total area of the respective region of interest of image j where $A_{d,j}$ and A_s were determined using an ImageJ algorithm.

3 Results and discussion

3.1 µCT analysis

The resulting 3D images of P1–5 obtained after applying the porosity detection algorithm (see Sect. 2.4) on the µCT data are depicted in Fig. 4a). The defect-free volume is hereby shown in transparent gray whereas the detected pores are colored according to their equivalent spherical pore diameter. The porosity is homogeneously distributed within the respective part volumes and it increases from P1 to P5 as expected owing to the variation in scan speed (see Table 1) intentionally introducing an increasing amount of lack of fusion porosity from P1 to P5 as the volumetric energy density $E_v = P_L \cdot (v_s \cdot h \cdot t_{l,n})^{-1}$ defined by Stoffregen et al. [33] decreases with increasing scan speed.

The relative densities of P1–5 were calculated by dividing the total pore volume by the total part volume and are visualized as a function of the scan speed in Fig. 4b). The results confirm that the relative part density decreases as the scan speed increases, i.e., from P1 to P5, which is in agreement with several studies [34–36]. The relative part densities of P1–5 cover a range of 99.0–99.9 %, i.e., the most interesting region of PBF-LB/M process window for structural applications, as porosity is typically minimized to avoid fatigue crack initiation [36, 37]. In Fig. 4c, d) the probability density functions of the equivalent spherical pore volume and the pore sphericity per part are visualized confirming that as the scan speed increases, the pore size increases and the pore sphericity decreases. This is due to the increased formation of larger lack of fusion pores which are typically larger and irregularly shaped compared to gas pores and keyhole pores [36, 38–41].

The layer-to-layer relative density ρ_s of each part P1–5 extracted from the µCT data according to the procedure described in Sect. 2.4 is plotted in Fig. 5. Hereby, ρ_s corresponds to the relative density of the material volume that was layerwise measured via ECT as discussed in Sect. 2.4.

The layer-to-layer relative densities ρ_s of P1–5 demonstrate that P1 has the highest relative density over the given layer range and the relative density decreases towards P4–5 as expected given the overall relative densities of the parts and the homogeneous distribution of pores within the parts (see Fig. 4a, b). The layer-to-layer gradient of the relative density is relatively constant for P1–3, but slightly positive for P4–5, i.e., the relative density increases with the layer number of these parts. Hence, the relative density of P4–5 is slightly higher at the top of the parts compared to the bottom of the parts. Furthermore, the layer-to-layer fluctuation of the relative density is very small for P1 and increases in direction to P5. This is partially owing to a narrower pore size distribution with a smaller average equivalent pore size for P1 which increases towards P5 (see Fig. 4c). Thus, porosity is most homogeneously distributed in P1 and the homogeneity decreases towards P5.

3.2 In-situ full-field IR monitoring

The part surfaces of P1–5 were monitored for the duration of the build cycle according to the procedure outlined in Sect. 2.1. Figure 6 depicts raw infrared camera images of the build scenario after the laser melting of the respective layers denoted in the images.

The images qualitatively demonstrate the heat up of the parts during the build cycle as the layer index increases which is in agreement with the findings of Williams et al. [26] for 316L stainless steel. Additionally, there is a region of the powder bed around each part which exhibits a considerably higher infrared radiation which is most pronounced at layer 1000. This is caused by ejected spatter particles during laser melting which are predominantly moved away from the part surface by the gas flow and land on the surrounding powder bed as shown in Fig. 7. Although the parts were molten by the laser sequentially in ascending order by part number, i.e., P1 first and P5 last, and the images were extracted after the melting of the respective layer of P5 was finished, and spatter ejected during the melting of P1 had the most time to cool, there is the considerably largest and hottest area with landed spatter particles in proximity to P1. This is probably owing to the relatively higher energy input owing to the lowest scan speed used to melt P1 (see Table 1) triggering an increased amount of spatter, which is in agreement with several studies on the influence process parameters on spatter formation mechanisms [42–44].

The part-wise temperature time series over the entire duration of the build cycle containing the average temperature of the regions illustrated by white squares in Fig. 6 were then extracted and converted to actual part surface

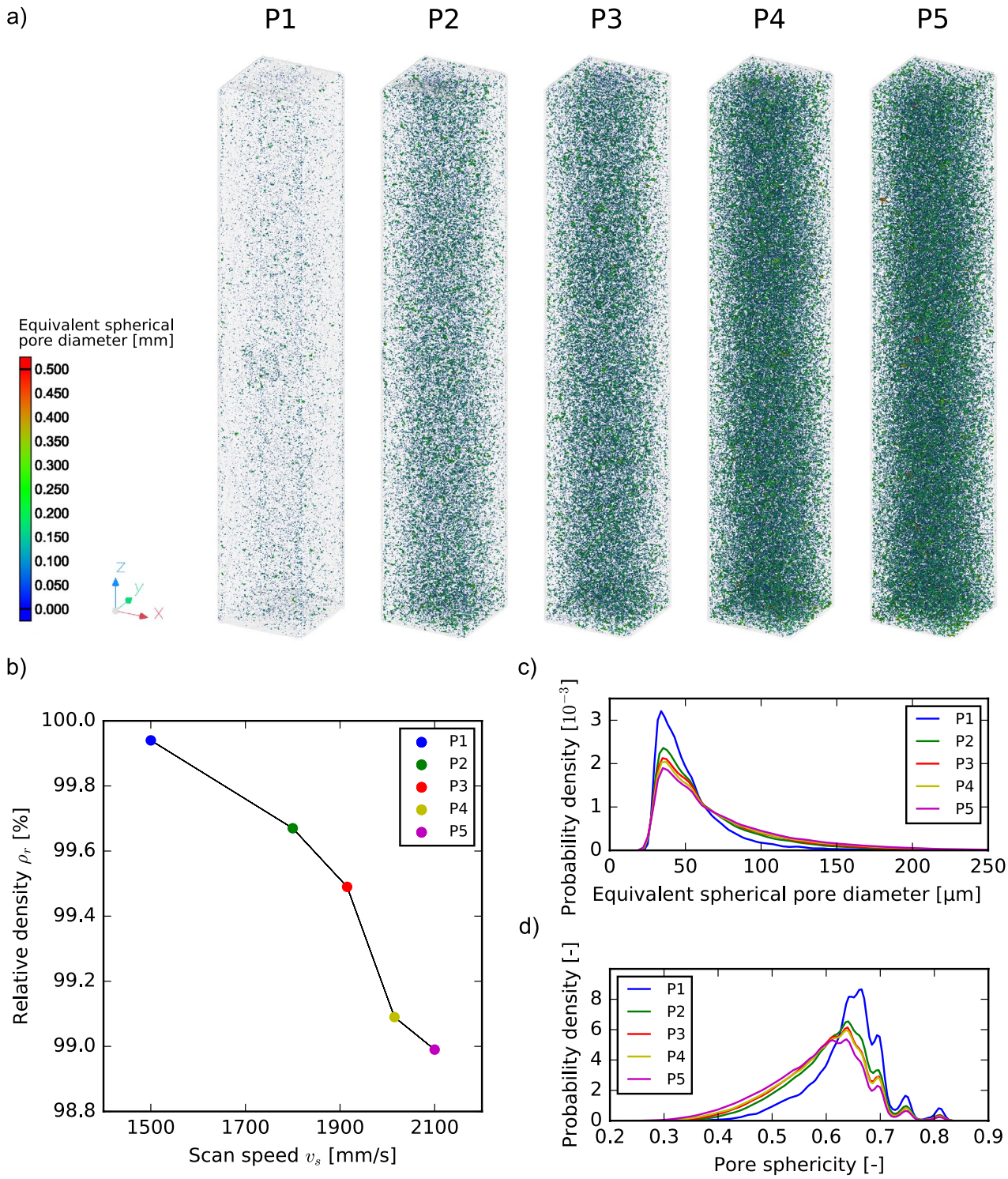

Fig. 4 **a** µCT images of the parts P1–5 where the part surfaces are depicted in transparent gray and the pores are colored according to their equivalent spherical diameter. **b** Relative density as a function of scan speed of P1–5 obtained by dividing the total pore volume per part by the respective total part volume. **c** Probability density functions of the equivalent spherical pore diameter of P1–5. d) Probability density functions of the pore sphericity of P1–5

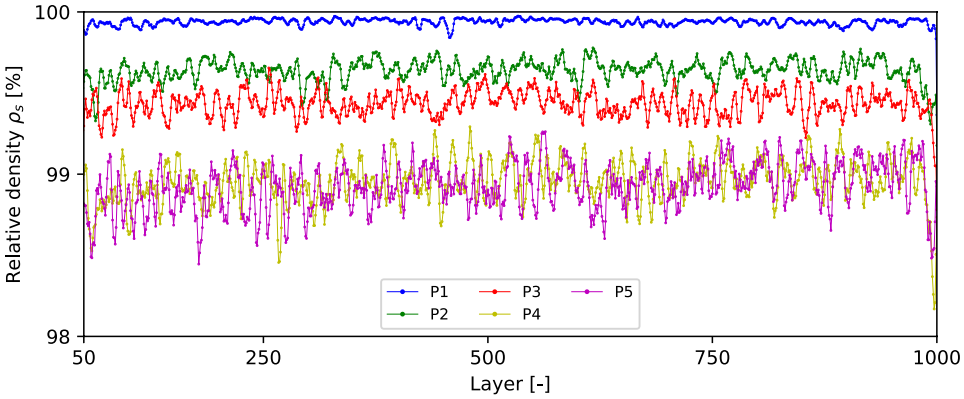

Fig. 5 Layerwise relative density ρ_s per part P1–5 computed based on the µCT data adopting the method described in Sect. 2.4. The relative density of each layer corresponds to the relative density of the material volume of the respective part that was layerwise measured via ECT during the PBF-LB/M build cycle as discussed in Sect. 2.4

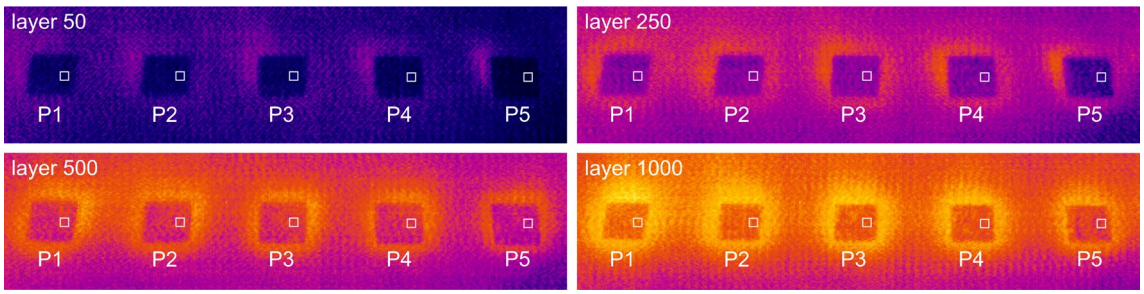

Fig. 6 Infrared camera images depicting the part surfaces after laser melting of the respective within the images denoted layers {50, 250, 500, 1000}. The white squares are the same regions as the ones used during calibration (see Sect. 2.3) which are used to calculate the average surface temperature per part. The quadratic part surfaces are distorted owing to the lens and the infrared camera positioning

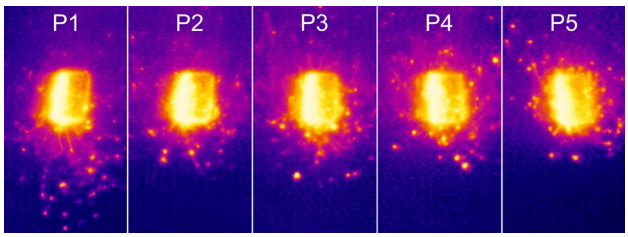

Fig. 7 Images depicting the part surfaces of P1–5 during laser melting of layer 500 of the build cycle extracted from the infrared camera video obtained during the PBF-LB/M build cycle

temperatures adopting the calibration functions according to Sect. 2.3. The time fraction of processing one layer of P1 is exemplarily shown in Fig. 8 where different events can be identified: the rapid temperature increase (1) occurs when the laser is melting the material followed by a rapid cool down which is characteristic for PBF-LB/M [4]. Subsequently, the recoater moves towards the powder piston obscuring the view of the camera coinciding with a small temperature peak (2) which is primarily owing to a change in emissivity as the recoater is made from different material, lies out of the focal plane of the infrared camera, among

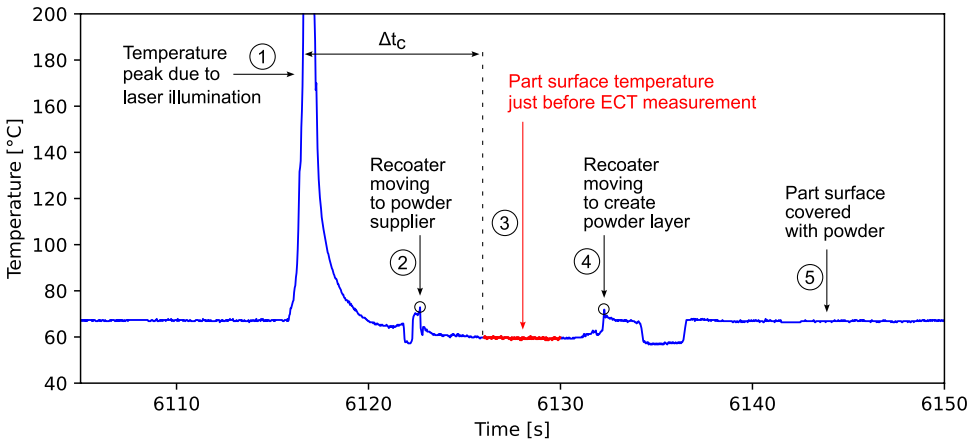

Fig. 8 Extraction of the part surface temperature T_S from the temperature time series acquired with the infrared camera during the PBF-LB/M build cycle, exemplary shown for the time fraction of processing a layer of P1. The depicted temperature was calibrated using the corresponding calibration function shown in Fig. 2c)

others. Then, the powder piston moves upwards and the recoater moves in the opposite direction to create the next powder layer. During this movement, the eddy current sensor moves ahead of the powder sequentially measuring P1–5 before they are covered by powder. Thus, the part surface temperature (3) is extracted right before the eddy current sensor mounted on the recoater obscures the camera view a second time indicated by the next small peak (4). Therefore, the temperature was extracted during 3 s before this peak occurs as indicated in red, and the part surface temperature T_S computed by averaging the temperature during the 3 s interval. After the powder recoating is completed, the parts are covered with powder (5) before the next layer cycle starts. An algorithm implemented in Python 3.9 was used to extract T_S accordingly for each layer and part, respectively.

The resulting part surface temperature T_S as a function of the layer index per part is plotted in Fig. 9. Notably, the periodicity, which is exemplarily shown in the zoomed window in the top left corner, coincides with the periodicity of the laser scan vector direction due to the adopted 90° alternating scan pattern (see Table 1). The scan vector direction influences the part surface profile and, therefore, the emissivity and the measured temperature as discussed in Sect. 2.3. Thus, the data were filtered with a moving average filter with a window size of 4 significantly reducing the noise; hence, the filtered data is used in the following analyses. T_S of all parts increases as a function of the layer index from about 55 °C to about 75 °C. This is due to the cold start of the PBF-LB/M build cycle, i.e., initially the build plate is at room temperature and the layer-to-layer heat input by the laser beam as discussed by Williams et al. [26] triggering the layer-to-layer increase of the part surface temperature as the material underneath is increasingly preheated. In comparison to the layer-to-layer increase of T_S, the part-to-part differences over the layer range are small, but significant (ANOVA, $F(4, 4995) = 42.12,\ p < 0.001$). Potential reasons for these differences are discussed in the following sections.

In order to compare the part-to-part differences, the mean temperature per part across the layer range $\bar{T}_S$ was calculated the resulting values are reported in Table 2, among others. The largest difference was found between P1 and P5 with $\Delta\bar{T}_S = 3.4\ °C$, which corresponds to the mean vertical offset between P1 and P5 in Fig. 9. Notably, the maximum part-to-part differences estimated by $\Delta\bar{T}_S$ are small compared to the maximum layer-to-layer difference in T_S of approximately 20 °C.

In general, part-to-part differences in $\bar{T}_S$ can be caused by different time delays Δt_c between the laser illumination and the ECT measurement, and different energy inputs expressed by E_v as a function of the process parameters. The extraction of Δt_c is exemplarily shown in Fig. 8 and the results presented in Table 2 demonstrating that there are differences of up to about 4 s in Δt_c among the parts owing to the illumination sequence of the parts. The parts are cooling down during Δt_c, thus the larger Δt_c, the longer the parts cool down until the ECT measurement is taken. This is in agreement with $\bar{T}_S$, which increases as Δt_c decreases; hence, the small differences in $\bar{T}_S$ could be caused by the difference in Δt_c owing to the illumination sequence of the parts.

Table 2 Volumetric energy density E_v, relative part density ρ_r, time delay Δt_c, and mean part surface temperature $\bar{T}_S$ per part

Part	E_v [J/mm^3]	ρ_r [%]	Δt_c [s]	$\bar{T}_S$ [$°C$]
P1	42.2	99.94	25.8	63.9
P2	35.2	99.67	24.8	65.7
P3	33.1	99.49	23.9	65.3
P4	31.4	99.09	22.8	66.7
P5	30.2	98.99	21.9	67.3

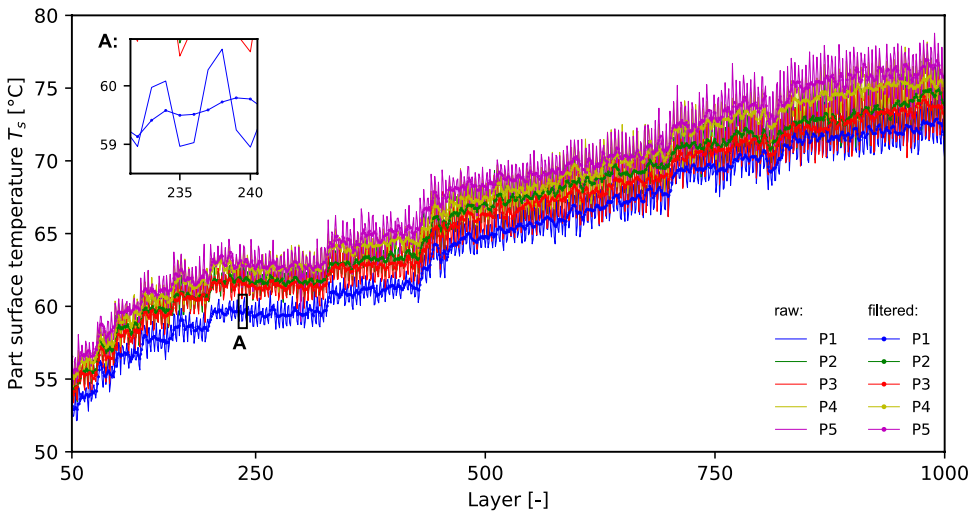

Fig. 9 Raw and filtered layer-wise part surface temperature T_S per part P1–5 extracted from the temperature time series. The data was filtered with a moving average filter with a window size of 4 to account for the periodicity (see zoomed window *A*) owing to the scan pattern. The standard deviations of T_S were neglected as $SD(T_S) < 1\ °C$ for all parts and layers and, therefore, omitted to increase the readability

The energy input as a function of the process parameters expressed by E_v is expected to be positively correlated to $\bar{T}_S$. However, the data presented in Table 2 demonstrates that $\bar{T}_S$ decreases as E_v increases; therefore, differences in E_v owing to process parameter variation obviously do not contribute to the differences in $\bar{T}_S$ among the parts. However, there are differences in thermal conductivity κ between the parts owing to the different relative densities triggered by the process parameters [45]. According to Butler et al. [45], porosity is inversely correlated with the thermal conductivity, i.e., the relative densities reported in Table 2 yield $\kappa_{P1} > \kappa_{P2} > \kappa_{P3} > \kappa_{P4} > \kappa_{P5}$. Thus, the differences in κ among the parts yield differences in the efficiency of the heat conduction from the part surface to the build plate influencing the part cooling during Δt_c potentially contributing to the differences in $\bar{T}_S$ among the parts.

Generally, the process parameters and illumination sequence only slightly affect T_S given the small part-to-part differences in T_S of maximum $\Delta\bar{T}_S = 3.4\,°C$. Layer-to-layer differences in T_S are, therefore, by far the more relevant regarding the disturbing influence of T_S on the in-situ ECT measurement.

3.3 Relative density monitoring via in-situ ECT

The layer-to-layer relative electrical conductivity σ_r of P1–5 obtained after processing the ECT data according to Sect. 2.2 is plotted in Fig. 10. The overall relative electrical conductivity σ_r per part reveals differences in electrical conductivity where P1 has the highest and P5 has the lowest electrical conductivity. According to Spurek et al. [18, 22], the relative electrical conductivity and the relative density are correlated. Although there are significant differences in σ_r between the parts at a given layer index as expected due to the difference in relative density (see Fig. 4b)), the layer-to-layer σ_r actually decreases with increasing layer number. This downward drift of σ_r is independent of the actual relative density because there is no drift in the layer-to-layer relative density as shown in Fig. 5. According to Bowler [27], the electrical conductivity of metals is inversely related to the part temperature, i.e., higher part temperatures at higher layer index yield lower electrical conductivities measured via ECT. Thus, the drift in σ_r is actually due to the increase in part surface temperature shown in Fig. 9 which decreases the actual layer-to-layer electrical conductivity of the near-surface fraction of the part volume at the moment the ECT measurement is conducted.

The strong correlation between the relative electrical conductivity and the relative density demonstrated by Spurek et al. [18, 22] allowed to establish a linear regression model to calibrate the ECT system to be able to measure the layer-to-layer relative density with high accuracy. In this context, the additional influence of the part temperature on the relative electrical conductivity acts as a disturbance: the linear regression predicting the relative density from the relative electrical conductivity is shown in Fig. 12a) indicating that there is a large fraction of the variance of σ_r over the layer range which is not explained by the corresponding relative density. The goodness of fit $R^2 = 0.548$ supports this observation demonstrating that in fact only about 55 % of the variance in ρ_s is explained by σ_r. The resulting regression function allows to predict $\hat{\rho}_s$ [%] from σ_r [%] according to

$$\hat{\rho}_s(\sigma_r) = 0.9737 \cdot \sigma_r + 2.3563 \tag{4}$$

The prediction accuracy is quantified by the mean absolute error (MAE) which is calculated according to

$$MAE = \frac{1}{n}\sum_{i=1}^{n} |\hat{\rho}_i - \rho_i| = 0.223\ \% \tag{5}$$

The MAE is defined as the average error between predicted value $\hat{\rho}$ and true value ρ in units of the predicted value, i.e., relative density [%]. Thus, the MAE demonstrates that the layer-to-layer relative density can be measured via ECT after calibration adopting the regression model according to Eq. (4) with an average error of 0.22 %. In comparison to Spurek et al. [22] where $MAE = 0.126$ %, the MAE obtained in this study is larger owing to the temperature drift in the ECT data caused by a layer-to-layer increase of T_S, where

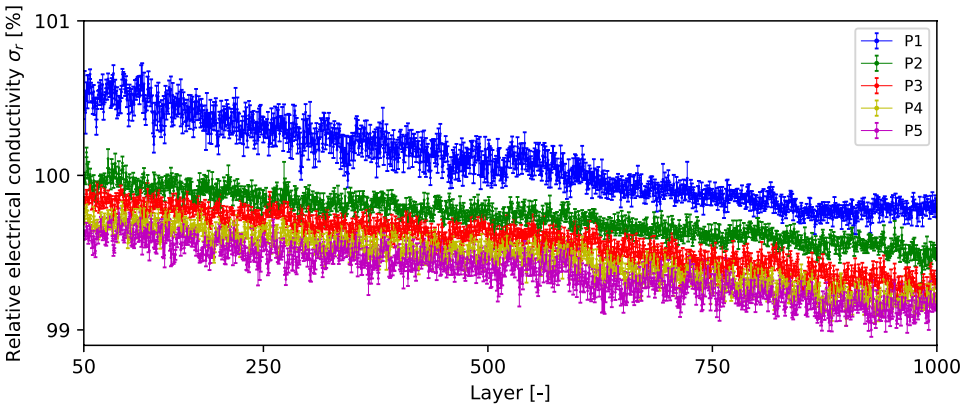

Fig. 10 Layerwise relative electrical conductivity σ_r (mean ± SD) calculated based on data acquired across $\Delta x_p = 3\,mm$ in the center of each part P1–5. The uncertainty due to ECT instrument noise was neglected ($U_I = 0.03$ %, expressed in units of σ_r) and, therefore, omitted to increase the readability. Therefore, the depicted standard deviations are due to actual within-layer material inhomogeneity

the total range of T_S is considerably larger owing to the part design.

Figure 11a–e depicts both the predicted layer-to-layer relative densities $\hat{\rho}_s(\sigma_r)$ for P1–5, obtained from Eq. (4), and the actual relative density ρ_s measured using µCT. As expected, the agreement between the predicted relative density $\hat{\rho}_s$ and the actual relative density ρ_s is not consistent across the layer range for all parts. This is due to the influence of the part temperature on the relative electrical conductivity of the parts which is not considered in the regression model according to Eq. (4) and, therefore, acts as a model disturbance. Neglecting the part temperature, therefore, leads to under- and overestimation of ρ_s for most of the layer range leading to the false conclusion that the drift in σ_r as a function of the layer index is caused by an actual vertical gradient in the relative density ρ_s, which is not the case as shown in Fig. 11.

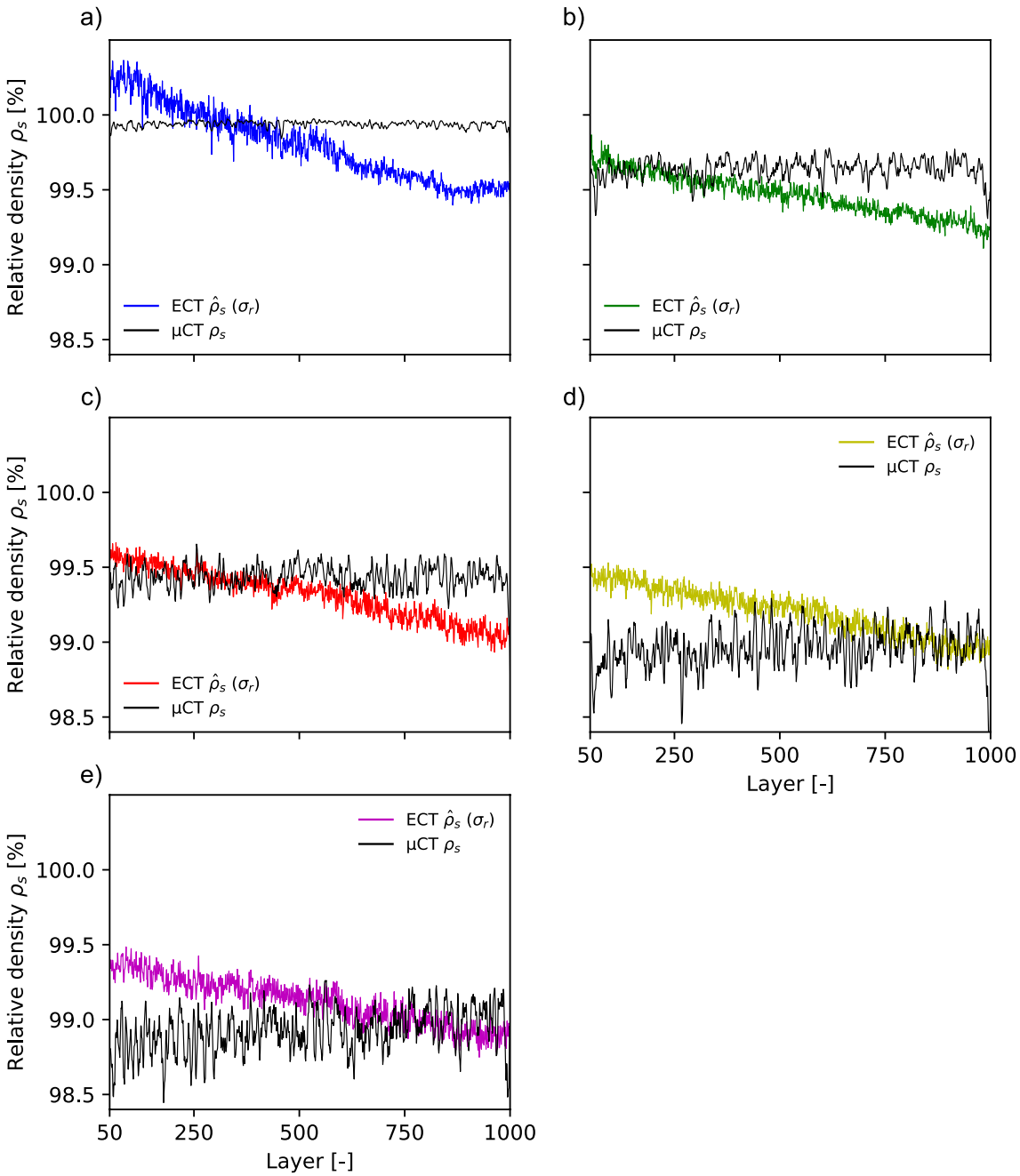

Fig. 11 Comparison between the predicted relative density $\hat{\rho}_s$, obtained from Eq. (4), and the actual relative density ρ_s of the corresponding slice measured via µCT according to Sect. 2.4 where a–e) depict P1–5, respectively

3.4 Temperature compensation

Temperature compensation methods adopted to reduce the temperature drift in electrical conductivity measurements conducted via ECT typically utilize the linear approximation of the temperature dependency of the electrical conductivity according to Eq. (1). In general, the linear approximation only holds for small changes in temperature as the temperature coefficient of the electrical conductivity changes as a function of temperature [46]. The relative electrical conductivity σ_r as a function of the part surface temperature T_S per part is shown in Fig. 12c). Given the small variation of relative density across the layer range (see Fig. 5), the corresponding influence of the relative density on the relative electrical conductivity is neglected. Thus, the good fit of the linear models to the respective data per part ($R^2 > 0.7$ for all

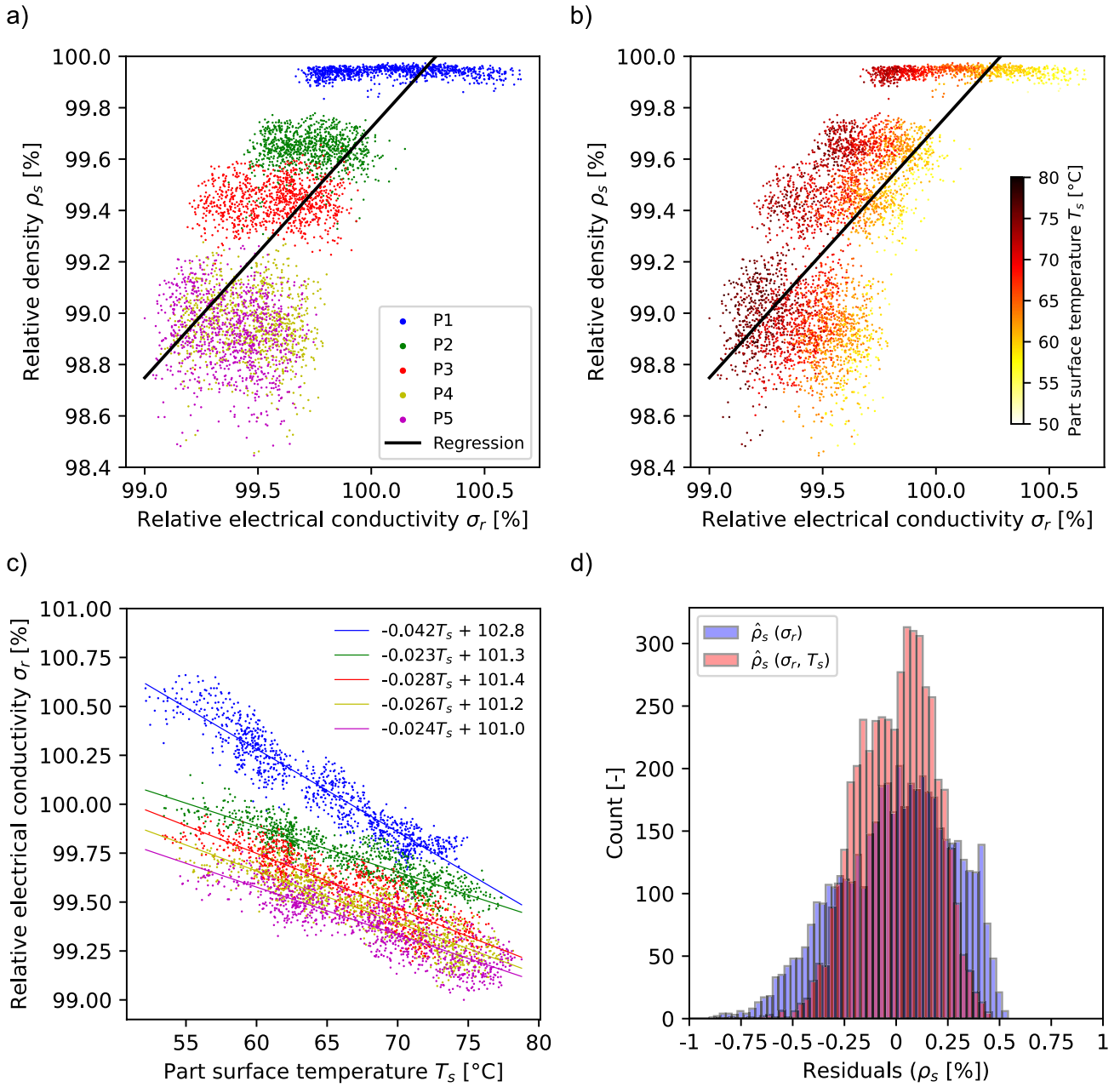

Fig. 12 **a** Least-square regression analysis between the relative electrical conductivity σ_r measured via ECT and the relative density ρ_s of the corresponding slice obtained by µCT analysis. **b** The same least-square regression analysis shown in **a** where the color of each point denotes the corresponding part surface temperature T_S according to the depicted color bar. **c** Least-square regression analysis between the relative electrical conductivity σ_r and the part surface temperature T_S. **d** Comparison of the residuals between the least-square regression model without temperature compensation $\hat{\rho}_s(\sigma_r)$ and with temperature compensation $\hat{\rho}_s(\sigma_r, T_S)$

parts) demonstrates that the linear approximation holds for the observed range of T_S.

In-situ monitoring of the relative part density via ECT requires the calibration of the specific ECT system for the alloy used adopting a linear model as demonstrated by Spurek et al. [18, 22]. These linear models are ideally experimentally obtained by in-situ monitoring of build cycles via ECT wherein test samples covering the region of interest in terms of relative density are fabricated and the relative density is subsequently measured via µCT. Due to the demonstrated linear relationship of the part temperature and the relative electrical conductivity, the temperature compensation is included in the linear model used for calibrating the ECT system, i.e., the relative density $\hat{\rho}_s$ [%] is predicted from the relative electrical conductivity σ_r [%] and the part surface temperature T_S [°C] according to

$$\hat{\rho}_s(\sigma_r, T_s) = 0.0507 \cdot T_s + 1.6024 \cdot \sigma_r - 63.6758 \tag{6}$$

Hereby, the linear regression model defined in Eq. (4) is extended to a multiple linear regression model according to Eq. (6) where the model is a least-square fitted plane in the 3D space defined by ρ_s, σ_r and T_S. In comparison to the model according to Eq. (4), the multiple linear regression model fits the data significantly better with $R^2 = 0.797$, i.e., about 80 % of the variance of ρ_s is explained by σ_r and T_S, which is similar to the results obtained by Spurek et al. [22]. To quantify the model accuracy, the MAE is calculated according to

$$MAE = \frac{1}{n} \sum_{i=1}^{n} |\hat{\rho}_i - \rho_i| = 0.15\ \% \tag{7}$$

The MAE is significantly improved compared to the model without temperature compensation where MAE = 0.223 % (see Eq. (5)), i.e., the accuracy of measuring the relative density via ECT expressed by the MAE is reduced by 32.7 % to 0.15 % relative density by means of the temperature compensation. The comparison of the model residuals expressed in relative density [%] of the model without temperature compensation $\hat{\rho}_s(\sigma_r)$ and with temperature compensation $\hat{\rho}_s(\sigma_r,\ T_S)$ is shown in Fig. 12d). Given the improvement of the accuracy expressed by the MAE, the distribution of the residuals of $\hat{\rho}_s(\sigma_r,\ T_S)$ is significantly narrower compared to $\hat{\rho}_s(\sigma_r)$ accordingly.

Figure 13a–e presents the predicted relative densities $\hat{\rho}_s(\sigma_r, T_S)$ for P1–5, obtained using Eq. (6), along with the actual density ρ_s that was measured using µCT. In comparison to Fig. 11 where the temperature drift was visible for all parts, there are no downward temperature drifts visible demonstrating the effectiveness of temperature compensation. For P2-5 shown in Fig. 13b–e, the agreement between $\hat{\rho}_s$ and ρ_s is very good, demonstrated by the small offset between the curves and similar layer-to-layer variation over the layer range which is most pronounced for P5 shown in Fig. 13e. Although the agreement for P1 depicted in Fig. 13a is good across the majority of the layer range, the model slightly overestimates the relative density at the lower end of the layer. Nevertheless, the presented method effectively compensates the temperature-induced drift in σ_r yielding a detection accuracy of 0.15 % relative density expressed by the MAE.

3.5 Implications for industrial use

In industry, in-situ ECT can be adopted for monitoring of co-built test specimens, which are manufactured alongside the actual parts, where the measured relative density is used to approve the batch of parts manufactured within the build cycle as part of quality control, e.g., in accordance with ASTM 52920 [47]. Hereby, the overall relative density of the co-built test specimen is relevant and is typically determined by conventional methods, such as the Archimedes method, microscopic analysis of cross-sections, or µCT. Table 3 presents the relative part density measured via µCT alongside the relative part density measured via ECT with and without temperature compensation, respectively. Notably, although the model with temperature compensation is slightly more accurate, it is not required in this case as the model without temperature compensation also allows to determine the relative part density with high accuracy.

In use cases where in-situ ECT is used to layerwise monitor the relative density, the risk of false interpretation of the measurement data owing to the temperature drift can lead to false alarms as $\hat{\rho}_s$ can fall below a defined quality threshold whereas the actual relative part density of the respective layer ρ_s is actually above the quality threshold. However, the temperature compensation method fed with experimental or simulated temperature data can effectively remove the temperature drift. Alternatively, a reference build cycle with the same configuration, where the required part quality was achieved, can be used to detect deviations.

Given the small temperature differences within the same layer as discussed in Sect. 3.2, the in-situ nondestructive inspection of parts with ECT is probably not significantly influenced by the temperature effect as in this case, the goal is to detect individual defects within otherwise mostly pore-free material of the same layer. Furthermore, the influence of the layer-to-layer temperature increase is probably small compared to the contrast between defects and the surrounding material and should, therefore, be easily distinguishable.

4 Conclusions

In this paper, the effect of temperature of PBF-LB/M-manufactured metallic parts on the determination of the relative part density through its response to an electromagnetic

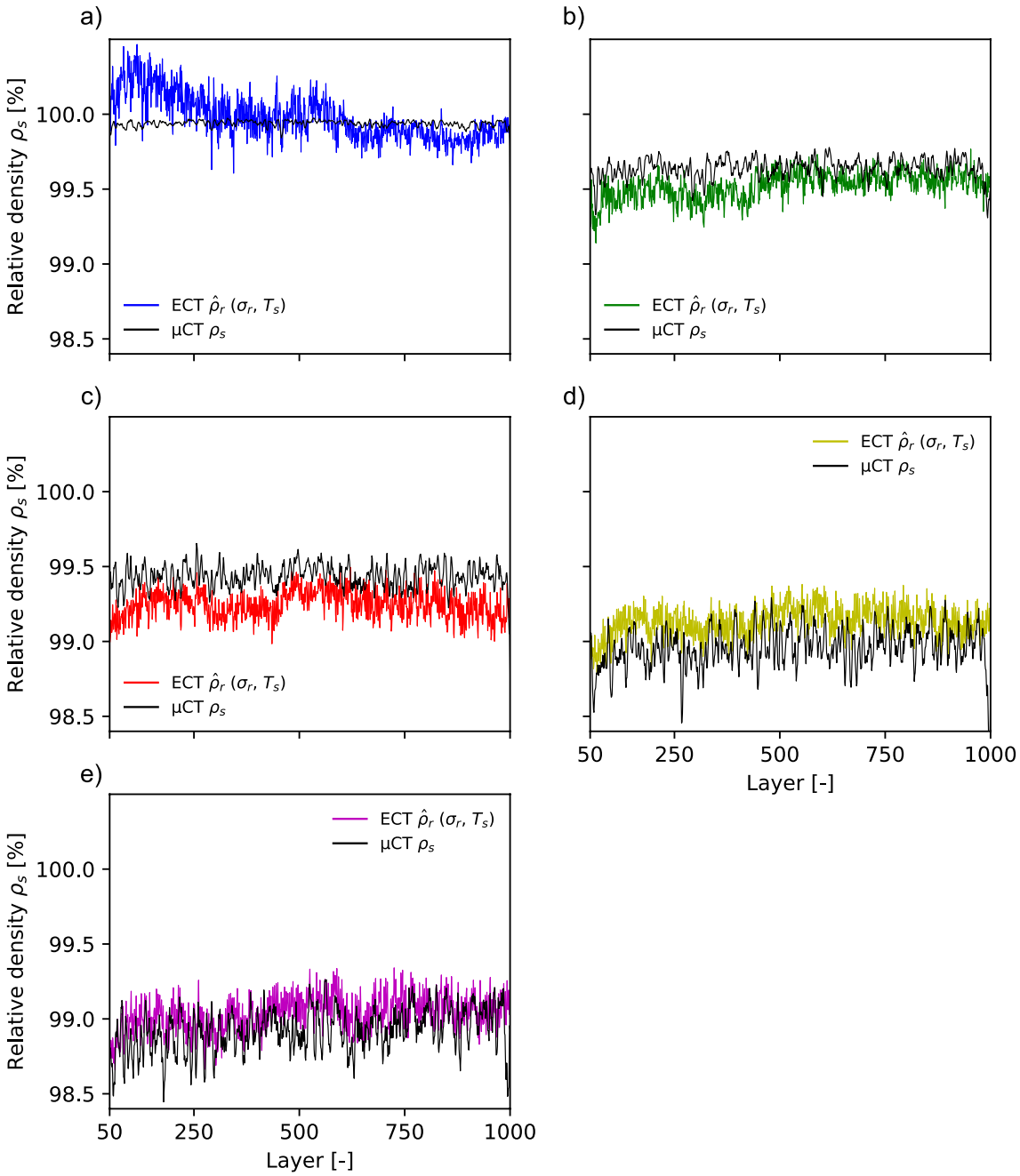

Fig. 13 Comparison between the layerwise relative density $\hat{\rho}_s$ predicted from the via ECT measured relative electrical conductivity σ_r adopting the linear regression model according to Eq. (6), and the layerwise relative density ρ_s of the corresponding slice measured via µCT according to Sect. 2.4 where **a**–**e** depict P1–5, respectively

excitation triggered by an ECT sensor was studied. It is of particular importance as the effective electromagnetic material properties, i.e., mainly the electrical conductivity for the non-magnetic material AlSi10Mg considered here, measured by the ECT sensor are affected both by the relative part density and part temperature, and part temperature variations are inherently occurring in PBF-LB/M. Therefore, the part temperatures were measured during the PBF-LB/M build cycle at the time of the in-situ ECT measurement, i.e., at each recoater crossing between layers, with a calibrated infrared camera. For the part temperature range observed within this study, it is confirmed that, as expected, the ECT response varies linearly with the part temperature. By applying a linear temperature compensation to the ECT signal, the mean average error of the layerwise measured relative density, which indicates the accuracy of determining the whole

Table 3 Relative density of the parts determined via µCT (ρ_r) and via in-situ ECT without temperature compensation ($\bar{\rho}_s(\sigma_r)$) and with temperature compensation ($\bar{\rho}_s(\sigma_r, T_S)$) where $\bar{\rho}_s$ was determined by averaging the layerwise acquired signals shown in Fig. 13

Part	ρ_r [%]	$\bar{\rho}_s(\sigma_r)$ [%]	$\Delta\rho_r$ [%]	$\bar{\rho}_s(\sigma_r, T_S)$ [%]	$\Delta\rho_r$ [%]
P1	99.94	99.80 ± 0.24	0.14	99.95 ± 0.16	0.01
P2	99.67	99.46 ± 0.14	0.21	99.51 ± 0.11	0.16
P3	99.49	99.31 ± 0.17	0.18	99.25 ± 0.12	0.24
P4	99.09	99.20 ± 0.16	0.11	99.14 ± 0.12	0.05
P5	98.99	99.12 ± 0.16	0.13	99.04 ± 0.13	0.05

part relative density, is reduced by a third: from 0.22% to 0.15%. The improvement is valuable for a better discrimination between different part qualities, and especially for the layer-by-layer evaluation of the relative density as it removes the temperature drift in the ECT signal triggered by the observed layer-by-layer increase of part temperature. The temperature effect on the measured ECT signal is not correlated with the part density, allowing for the simple compensation scheme proposed in this study.

Another important finding is that the volumetric energy density, herein varied by selecting different scan speeds, and the illumination sequence, i.e., the order in which the laser illuminates the different parts on the build plate, have a negligible impact on the part temperature during the recoater crossing when an in-situ ECT measurement is conducted, the final part temperature, as well as the overall temperature variation during the build job. To be precise, the time delay between the laser illumination and the in-situ ECT measurement has a perceptible but small effect on the part surface temperature. For the experiments conducted in this study, the by far most relevant temperature variation is the layer-by-layer part temperatures increase from about 55°C to 75°C irrespective of the part position on the build plate and the applied process parameters. It means that, for a given part geometry, the temperature compensation parameters could be established once from a good fabrication without requiring the installation of any temperature sensors. For an additional level of sophistication, the routinely performed thermal simulations, i.e., for the evaluation of residual-stress-induced part deformations, could be used to give an input to the temperature compensation algorithm. Nevertheless, if a temperature sensor is available on the PBF-LB/M machine, its output can be used but the results demonstrate that this should not be necessary in most industrial use cases.

Author Contributions Marvin A. Spurek: conceptualization, methodology, software, validation, formal analysis, investigation, writing—original draft, writing—review and editing. Adriaan B. Spierings: writing—review and editing, supervision, funding acquisition. Marc Lany: writing—review and editing. Bernard Revaz: writing—review and editing, funding acquisition. Gilles Santi: software, writing—review and editing. Jonatan Wicht: software, writing—review and editing. Konrad Wegener: writing—review and editing, supervision, resources.

Funding Open access funding provided by Swiss Federal Institute of Technology Zurich. Open Access funding provided by ETH Zurich. This work was supported by the Swiss Innovation Agency Innosuisse [grant number 33657.1].

Availability of data, code and material This will be made available upon reasonable request.

Declarations

Conflict of interest The authors declare that there is no conflict of interest regarding the publication of this article.

References

1. Wohlers Terry (2021) Wohlers report 2021: 3D printing and additive manufacturing: global state of the industry. Wohlers Associates, Fort Collins, Colorado. 9780991333271
2. Culmone Costanza, Smit Gerwin, Breedveld Paul (2019) Additive manufacturing of medical instruments: A state-of-the-art review. Additive Manufacturing, 27 (April): 461–473, 5. ISSN 22148604. https://doi.org/10.1016/j.addma.2019.03.015. https://linkinghub.elsevier.com/retrieve/pii/S2214860418308911
3. Blakey-Milner Byron, Gradl Paul, Snedden Glen, Brooks Michael, Pitot Jean, Lopez Elena, Leary Martin, Berto Filippo, Plessis Anton du (2021) Metal additive manufacturing in aerospace: A review. Materials and Design, 209 (July): 110008. ISSN 18734197. https://doi.org/10.1016/j.matdes.2021.110008. https://doi.org/10.1016/j.matdes.2021.110008
4. Wei HL, Mukherjee T, Zhang W, Zuback JS, Knapp GL, De A, DebRoy T (2021) Mechanistic models for additive manufacturing of metallic components. Progress in Materials Science, 116 (June 2020): 100703, 2. ISSN 00796425. https://doi.org/10.1016/j.pmatsci.2020.100703. https://linkinghub.elsevier.com/retrieve/pii/S0079642520300670
5. Plessis Anton du, Yadroitsev Igor, Yadroitsava Ina, Le Roux Stephan G (2018) X-Ray Microcomputed Tomography in Additive Manufacturing: A Review of the Current Technology and Applications. 3D Printing and Additive Manufacturing, 5 (3): 227–247, 9. ISSN 2329-7662. https://doi.org/10.1089/3dp.2018.0060. https://www.liebertpub.com/doi/10.1089/3dp.2018.0060
6. DebRoy T, Wei HL, Zuback JS, Mukherjee T, Elmer JW, Milewski JO, Beese AM, Wilson-Heid A, De A, Zhang W (2018) Additive manufacturing of metallic components - Process, structure and properties. Progress in Materials Science, 92: 112–224, 3 . ISSN

00796425. https://doi.org/10.1016/j.pmatsci.2017.10.001. https://linkinghub.elsevier.com/retrieve/pii/S0079642517301172
7. Grasso M, Remani A, Dickins A, Colosimo BM, Leach RK (2021) In-situ measurement and monitoring methods for metal powder bed fusion: an updated review. Measurement Science and Technology, 32 (11): 112001, 11 . ISSN 0957-0233. https://doi.org/10.1088/1361-6501/ac0b6b. https://iopscience.iop.org/article/10.1088/1361-6501/ac0b6b
8. American Society for Testing and Materials (ASTM). ASTM E3166-20: Standard Guide for Nondestructive Examination of Metal Additively Manufactured Aerospace Parts After Build. ASTM International, (2020). https://doi.org/10.1520/E3166-20E01.1.14
9. Guo Sai, Ren Guanhui, Zhang Bi (2021) Subsurface Defect Evaluation of Selective-Laser-Melted Inconel 738LC Alloy Using Eddy Current Testing for Additive/Subtractive Hybrid Manufacturing. Chinese Journal of Mechanical Engineering, 34 (1): 111, 12 . ISSN 1000-9345. https://doi.org/10.1186/s10033-021-00633-9. https://cjme.springeropen.com/articles/10.1186/s10033-021-00633-9
10. Kobayashi Noriyasu, Yamamoto Setsu, Sugawara Azusa, Nakane Masayo, Tsuji Daisuke , Hino Takehisa, Terada Takahiro, Ochiai Makoto (2019) Fundamental experiments of eddy current testing for additive manufacturing metallic material toward in-process inspection. In AIP Conference Proceedings, volume 2102, page 070003, . ISBN 9780735418325. https://doi.org/10.1063/1.5099803. http://aip.scitation.org/doi/abs/10.1063/1.5099803
11. Ehlers Henrik, Pelkner Matthias, Thewes Roland (2020) Heterodyne Eddy Current Testing Using Magnetoresistive Sensors for Additive Manufacturing Purposes. IEEE Sensors Journal, 20 (11): 5793–5800, 6 . ISSN 1530-437X. https://doi.org/10.1109/JSEN.2020.2973547. https://ieeexplore.ieee.org/document/8995500/
12. Hippert David Florian (2015)High resolution eddy current inspection and eddy current testing for additive manufacturing. PhD thesis, EPFL Lausanne,
13. Hippert David, Jhabvala Jamasp, Boillat Eric, Santi Gilles, Bleuler Hannes (2015)Development of an Eddy current testing method as process control for additive manufacturing of metallic components. 2015 IFToMM World Congress Proceedings, IFToMM 2015, pages 10–14, . https://doi.org/10.6567/IFToMM.14TH.WC.OS20.022
14. Duarte Valdemar R, Rodrigues Tiago A, Machado Miguel A, Pragana João PM, Pombinha Pedro, Coutinho Luísa, Silva Carlos MA, Miranda Rosa M, Goodwin Carley, Huber Daniel E, Oliveira Joao P, Santos Telmo G (2021) Benchmarking of Non-destructive Testing for Additive Manufacturing. 3D Printing and Additive Manufacturing, 8 (4): 263–270, 8 . ISSN 2329-7662. https://doi.org/10.1089/3dp.2020.0204. https://www.liebertpub.com/doi/10.1089/3dp.2020.0204
15. Sheng Bojie, Kanfoud Jamil, Gan Tat-Hean (2022) Quality Control of Metal Additive Manufacturing. In Prof. Igor V Shishkovsky, editor, Advanced Additive Manufacturing, chapter 5. IntechOpen, Rijeka, . https://doi.org/10.5772/intechopen.103121. https://doi.org/10.5772/intechopen.103121
16. Farag Heba E, Toyserkani Ehsan, Khamesee Mir Behrad (2022) Non-Destructive Testing Using Eddy Current Sensors for Defect Detection in Additively Manufactured Titanium and Stainless-Steel Parts. Sensors, 22 (14): 5440, 7 . ISSN 1424-8220. https://doi.org/10.3390/s22145440. https://www.mdpi.com/1424-8220/22/14/5440
17. Geľatko Matüš, Hatala Michal, Botko František, Vandžura Radoslav, Hajnyš Jiří (2022) Eddy Current Testing of Artificial Defects in 316L Stainless Steel Samples Made by Additive Manufacturing Technology. Materials, 15 (19): 6783, 9 . ISSN 1996-1944. https://doi.org/10.3390/ma15196783. https://www.mdpi.com/1996-1944/15/19/6783
18. Spurek Marvin Aaron, Luong Viet Hiep, Spierings Adriaan Bernardus, Lany Marc, Santi Gilles, Revaz Bernard, Wegener Konrad (2021) Relative Density Measurement of PBF-Manufactured 316L and AlSi10Mg Samples via Eddy Current Testing. Metals, 11 (9): 1376, 8 . ISSN 2075-4701. https://doi.org/10.3390/met11091376. https://www.mdpi.com/2075-4701/11/9/1376
19. D'Accardi Ester, Krankenhagen Rainer, Ulbricht Alexander, Pelkner Matthias, Pohl Rainer, Palumbo Davide, Galietti Umberto (2022) Capability to detect and localize typical defects of laser powder bed fusion (L-PBF) process: an experimental investigation with different non-destructive techniques. Progress in Additive Manufacturing, 7 (6): 1239–1256, 12 . ISSN 2363-9512. https://doi.org/10.1007/s40964-022-00297-4. https://link.springer.com/10.1007/s40964-022-00297-4
20. Eisenbarth Daniel, Stoll Philipp, Klahn Christoph, Heinis Timon B, Meboldt Mirko, Wegener Konrad (2020) Unique coding for authentication and anti-counterfeiting by controlled and random process variation in L-PBF and L-DED. Additive Manufacturing, 35 (January): 101298, 10 . ISSN 22148604. https://doi.org/10.1016/j.addma.2020.101298. https://linkinghub.elsevier.com/retrieve/pii/S2214860420306709
21. Todorov Evgueni I, Boulware Paul, Gaah Kingsley (2018) Demonstration of array eddy current technology for real-time monitoring of laser powder bed fusion additive manufacturing process. In Peter J. Shull, editor, Nondestructive Characterization and Monitoring of Advanced Materials, Aerospace, Civil Infrastructure, and Transportation XII, volume 1059913, page 40. SPIE, 3 . ISBN 9781510616943. https://doi.org/10.1117/12.2297511. https://www.spiedigitallibrary.org/conference-proceedings-of-spie/10599/2297511/Demonstration-of-array-eddy-current-technology-for-real-time-monitoring/10.1117/12.2297511.full
22. Spurek Marvin A, Spierings Adriaan B, Lany Marc, Revaz Bernard, Santi Gilles, Wicht Jonatan, Wegener Konrad (2022) In-situ monitoring of powder bed fusion of metals using eddy current testing. Additive Manufacturing, 60 (PB): 103259, . ISSN 22148604. https://doi.org/10.1016/j.addma.2022.103259. https://doi.org/10.1016/j.addma.2022.103259
23. Ehlers Henrik, Pelkner Matthias, Thewes Roland (2022) Online Process Monitoring for Additive Manufacturing Using Eddy Current Testing With Magnetoresistive Sensor Arrays. IEEE Sensors Journal, 22 (20): 19293–19300, 10 . ISSN 1530-437X. https://doi.org/10.1109/JSEN.2022.3205177. https://ieeexplore.ieee.org/document/9892689/
24. Chen Yao, Peng Xing, Kong Lingbao, Dong Guangxi, Remani Afaf, Leach Richard (2021)Defect inspection technologies for additive manufacturing. International Journal of Extreme Manufacturing, 3 (2): 022002, 4 . ISSN 2631-8644. https://doi.org/10.1088/2631-7990/abe0d0. https://iopscience.iop.org/article/10.1088/2631-7990/abe0d0
25. Mukherjee T, DebRoy T (2019) A digital twin for rapid qualification of 3D printed metallic components. Applied Materials Today, 14: 59–65, ISSN 23529407. https://doi.org/10.1016/j.apmt.2018.11.003. https://doi.org/10.1016/j.apmt.2018.11.003
26. Williams Richard J, Piglione Alessandro, Rønneberg Tobias, Jones Connor, Pham Minh-Son, Davies Catrin M, Hooper Paul A (2019) In situ thermography for laser powder bed fusion: Effects of layer temperature on porosity, microstructure and mechanical properties. Additive Manufacturing, 30 (March): 100880, 12 . ISSN 22148604. https://doi.org/10.1016/j.addma.2019.100880. https://linkinghub.elsevier.com/retrieve/pii/S2214860419303410
27. Bowler Nicola (2019) Eddy-Current Nondestructive Evaluation. Springer Series in Measurement Science and Technology. Springer, New York, New York, NY
28. Silbernagel Cassidy, Ashcroft Ian, Dickens Phill, Galea Michael (2018) Electrical resistivity of additively manufactured AlSi10Mg for use in electric motors. Additive Manufacturing, 21 (March):

395–403, ISSN 22148604. https://doi.org/10.1016/j.addma.2018.03.027. https://doi.org/10.1016/j.addma.2018.03.027
29. Williams Richard J, Davies Catrin M, Hooper Paul A (2021) In situ monitoring of the layer height in laser powder bed fusion. Material Design and Processing Communications, 3 (6): 3–7, . ISSN 25776576. https://doi.org/10.1002/mdp2.173
30. García-Martín Javier, Gómez-Gil Jaime, Vázquez-Sánchez Ernesto (2011) Non-Destructive Techniques Based on Eddy Current Testing. Sensors, 11 (3): 2525–2565, 2 ISSN 1424-8220. https://doi.org/10.3390/s110302525. http://www.mdpi.com/1424-8220/11/3/2525
31. GUM. Evaluation of measurement data – Guide to the expression of uncertainty in measurement. International Organization for Standardization Geneva ISBN, 50 (September): 134, (2008). ISSN 00099147. http://www.bipm.org/en/publications/guides/gum.html
32. Bramson MA (1968) Infrared Radiation: A Handbook for Applications. Plenum Press, Optical physics and engineering
33. Siedelhofer C, Abele E, Stoffregen H, Fischer J (2011) Selective laser melting of porous structures. Proceedings of the 22th International Solid Freeform Fabrication Symposium, 19 (4): 680-695. https://doi.org/10.3724/SP.J.1042.2011.00580
34. Kasperovich Galina, Haubrich Jan, Gussone Joachim, Requena Guillermo (2016) Corrigendum to "Correlation between porosity and processing parameters in TiAl6V4 produced by selective laser melting" [Materials and Design 105 (2016) 160-170]. Materials & Design, 112: 160–161, 12. ISSN 02641275. https://doi.org/10.1016/j.matdes.2016.09.040. https://linkinghub.elsevier.com/retrieve/pii/S026412751631214X
35. Sola Antonella, Nouri Alireza (2019) Microstructural porosity in additive manufacturing: The formation and detection of pores in metal parts fabricated by powder bed fusion. Journal of Advanced Manufacturing and Processing, 1 (3): 1–21, 7. ISSN 2637-403X. https://doi.org/10.1002/amp2.10021. https://onlinelibrary.wiley.com/doi/10.1002/amp2.10021
36. Yang Kun V, Rometsch Paul, Jarvis Tom, Rao Jeremy, Cao Sheng, Davies Chris, Wu Xinhua (2018) Porosity formation mechanisms and fatigue response in Al-Si-Mg alloys made by selective laser melting. Materials Science and Engineering: A, 712 (September 2017): 166–174, 1. ISSN 09215093. https://doi.org/10.1016/j.msea.2017.11.078. https://linkinghub.elsevier.com/retrieve/pii/S0921509317315393
37. Seifi Mohsen, Salem Ayman, Beuth Jack, Harrysson Ola, Lewandowski John J (2016) Overview of Materials Qualification Needs for Metal Additive Manufacturing. JOM, 68 (3): 747–764, 3. ISSN 1047-4838. https://doi.org/10.1007/s11837-015-1810-0. http://link.springer.com/10.1007/s11837-015-1810-0
38. Carlton Holly D, Haboub Abdel, Gallegos Gilbert F, Parkinson Dilworth Y, A Alastair (2016) MacDowell. Damage evolution and failure mechanisms in additively manufactured stainless steel. Materials Science and Engineering A, 651: 406–414. ISSN 09215093. https://doi.org/10.1016/j.msea.2015.10.073. http://dx.doi.org/10.1016/j.msea.2015.10.073
39. Choo Hahn, Sham Kin-Ling, Bohling John, Ngo Austin, Xiao Xianghui, Ren Yang, Depond Philip J, Matthews Manyalibo J, Garlea Elena (2019) Effect of laser power on defect, texture, and microstructure of a laser powder bed fusion processed 316L stainless steel. Materials & Design, 164: 107534, 2. ISSN 02641275. https://doi.org/10.1016/j.matdes.2018.12.006. https://linkinghub.elsevier.com/retrieve/pii/S0264127518308773
40. Ngnekou Julius N. Domfang, Nadot Yves, Henaff Gilbert, Nicolai Julien, Ridosz, Lionel (2017) Influence of defect size on the fatigue resistance of AlSi10Mg alloy elaborated by selective laser melting (SLM). Procedia Structural Integrity, 7: 75–83, ISSN 24523216. https://doi.org/10.1016/j.prostr.2017.11.063. https://doi.org/10.1016/j.prostr.2017.11.063
41. Bayat Mohamad, Mohanty Sankhya, Hattel Jesper Henri (2019) Multiphysics modelling of lack-of-fusion voids formation and evolution in IN718 made by multi-track/multi-layer L-PBF. International Journal of Heat and Mass Transfer, 139: 95–114, 8 ISSN 00179310. https://doi.org/10.1016/j.ijheatmasstransfer.2019.05.003. https://linkinghub.elsevier.com/retrieve/pii/S0017931018351020
42. Taheri Andani Mohsen, Dehghani Reza, Karamooz-Ravari Mohammad Reza, Mirzaeifar Reza, Ni Jun (2018) A study on the effect of energy input on spatter particles creation during selective laser melting process. Additive Manufacturing, 20: 33–43, 3. ISSN 22148604. https://doi.org/10.1016/j.addma.2017.12.009. https://linkinghub.elsevier.com/retrieve/pii/S2214860417304529
43. Gunenthiram V, Peyre P, Schneider M, Dal M, Coste F, Koutiri I, Fabbro R (2018) Experimental analysis of spatter generation and melt-pool behavior during the powder bed laser beam melting process. Journal of Materials Processing Technology, 251 (August 2017): 376–386, 1. ISSN 09240136. https://doi.org/10.1016/j.jmatprotec.2017.08.012. https://linkinghub.elsevier.com/retrieve/pii/S0924013617303606
44. Liu Yang, Yang Yongqiang, Mai Shuzhen, Wang Di, Song Changhui (2015) Investigation into spatter behavior during selective laser melting of AISI 316L stainless steel powder. Materials and Design, 87: 797–806. ISSN 18734197. https://doi.org/10.1016/j.matdes.2015.08.086
45. Butler C, Babu S, Lundy R, O'Reilly Meehan R, Punch J, Jeffers N (2021) Effects of processing parameters and heat treatment on thermal conductivity of additively manufactured AlSi10Mg by selective laser melting. Materials Characterization, 173 (January): 110945, ISSN 10445803. https://doi.org/10.1016/j.matchar.2021.110945. https://doi.org/10.1016/j.matchar.2021.110945
46. Kasap S (2000) Principles of Electrical Engineering Materials and Devices. McGraw Hill, Electrical & electronic series
47. American Society for Testing and International organization for standardization Materials (ASTM); (ISO). ISO/ASTM DIS 52920:2021. (August), (2021)